Engineering the defect distribution via boron doping in amorphous TiO$_2$ for robust photocatalytic NO removal

Hongbao Jia [a], Huan Shang [a,*], Yue He [a], Shuwei Gu [a], Shuangjun Li [b], Qing Wang [b], Shike Wang [b], Jinghuan Peng [a], Xichen Feng [a], Pengpeng Li [a], Hui Xu [a], Chengliang Mao [c], Hao Li [d], Shuning Xiao [a], Ding Wang [a], Guisheng Li [a,b], Dieqing Zhang [b,*]

[a] School of Materials and Chemistry, University of Shanghai for Science and Technology, Shanghai 200093, PR China
[b] The Education Ministry Key Lab of Resource Chemistry, Joint International Research Laboratory of Resource Chemistry of Ministry of Education, Shanghai Key Laboratory of Rare Earth Functional Materials, and Shanghai Frontiers Science Center of Biomimetic Catalysis, Shanghai Normal University, Shanghai 200234, PR China
[c] Department of Chemistry, University of Toronto, Toronto, ON M5S 3H6, Canada
[d] School of Environmental Science and Engineering, Shanghai Jiao Tong University, Shanghai 200240, PR China

ARTICLE INFO

ABSTRACT

Nitric oxide (NO) pollutant can threaten the regional environment and human health. Solar-powered photocatalytic oxidation method is desirable for NO removal (ppb level) at ambient conditions, but suffers from the unsatisfactory activity and poor selectivity due to the sluggish molecular oxygen activation. Herein, we demonstrate that efficient photocatalytic NO removal can be realized by modulating the defects distribution of amorphous TiO$_2$ via boron doping. Theoretical calculations and experimental results reveal that H$_3$BO$_3$ modification can refine the structure of surface oxygen vacancies, promoting electron-rich molecular oxygen activation to •OH. Meanwhile, bulk-phase oxygen defects can be filled by free-state B atoms, accelerating the electron transfer via Ti-O-B bonding. Homogeneous boron-doped amorphous TiO$_2$ achieves about 5 times higher NO removal efficiency (~50%) than that of amorphous TiO$_2$ (~9%) without releasing remarkable NO$_2$ (selectivity, ~97%). This study provides a state-of-the-art approach for robust photocatalytic NO removal by engineering the defect distribution.

1. Introduction

Nitrogen oxides (NO$_x$) is a typical atmospheric pollutant that causes serious environmental pollution such as acid rain, haze, and photochemical smog [1–3]. In atmospheric reactions, dilute NO$_x$ (ppb) can react with the reactive oxygen radical to form O$_3$ and PM$_{2.5}$, which threatens the human health [4–7]. Photocatalysis has been considered as a feasible technology for NO$_x$ treatment due to its sustainability and availability compared with the traditional selective reduction reaction process [8,9]. However, photocatalytic NO oxidation reaction still suffers from the unsatisfactory activity and poor selectivity.

Extensive researches have highlighted that photocatalytic NO oxidation reaction is determinately dominated by reactive oxygen species (ROS) produced by molecular oxygen activation/reduction [10–12]. These ROS can convert NO into nitrate and hazardous by-product NO$_2$, affecting the selectivity of NO oxidation removal [13,

14]. For example, Zhang's group manipulated the generation of side-on •O$_2^-$ by constructing oxygen vacancies on the surface of BiOCl (001), achieving the complete NO oxidation (NO + •O$_2^-$ → NO$_3^-$) [15]. Meanwhile, end-on •O$_2^-$ preferred to oxidize NO to NO$_2$/NO$_2^-$. That is, the selectivity of nitrate is dependent on the adsorption mode of O$_2$ in •O$_2^-$-mediated NO oxidation, suggesting that the precise regulation of ROS can be feasible to achieve selective oxidation of NO. But, singlet oxygen (^{1}O$_2$) is also a common ROS, accompanied by the molecular oxygen activation reaction, which preferentially converts NO to NO$_2$ due to its feeble oxidizing capacity (2NO + ^{1}O$_2$ → 2NO$_2$) [16]. Comparing with these diatomic oxygen species, hydroxyl radicals (•OH) can selectively oxidize NO to nitrate through the continuous oxidation reactions, which is independent on the configuration of ROS. Moreover, •OH can coordinate with ^{1}O$_2$ to convert NO into nitrate (2NO + 2•OH + ^{1}O$_2$ → 2NO$_3^-$ + 2 H$^+$), remedying for the weak oxidation of ^{1}O$_2$ [16]. Therefore, selective generation of •OH could achieve the deep

---

* Corresponding authors.
  E-mail addresses: huanshang1992@163.com (H. Shang), dqzhang@shnu.edu.cn (D. Zhang).

photocatalytic oxidation of NO and suppress the formation of NO_2.

Given that $\bullet OH$ can be derived from H_2O_2 decomposition ($H_2O_2 + e^- + H^+ \rightarrow \bullet OH + H_2O$), fine-tuning the reaction site to activate molecular oxygen for the production of H_2O_2 can direct the generation of $\bullet OH$ [17, 18]. Defect engineering is often applied to facilitate the two-electron molecular oxygen activation by adjusting the atomic arrangement and electronic structure of the catalysts [19–21]. Typically, amorphous photocatalyst with abundant defective sites can be the potential candidate for the defect-engineering molecular oxygen activation to $\bullet OH$, where surface unsaturated defects are favorable for the adsorption and activation of O_2 with efficient electronic utilization [22]. But coin has two sides. The bulk-phase oxygen defect on amorphous catalysts may lead to fast recombination of photogenerated carriers due to their long-range disordered atomic structure, further deteriorating photocatalytic activity [23,24].

Herein, we report that this bottleneck of amorphous catalysts for NO removal can be well surmounted by modulating their oxygen defect distribution via boron doping. As a proof of concept, homogeneous boron-doped amorphous TiO_2 (HB-TiO_2) is employed as a model catalyst for NO oxidation. Theoretical calculations and experimental results reveal that the surface oxygen vacancies can be refined by the H_3BO_3 modification, where BO_3^- can facilitate the electron transfer to surface defects (Ti^{3+}) for O_2 reduction. Meanwhile, the bulk-phase oxygen defects can be filled by free-state B atoms, accelerating electron transfer from neighboring Ti^{3+} to B through forming the Ti-O-B bonding. Filling bulk-phase oxygen defects can inhibit the recombination of photogenerated electrons and holes due to localized electron aggregation within bulk-phase defects. As a result, HB-TiO_2 possesses a higher NO removal efficiency (50%) under visible light irradiation, which is about 5 times higher than that of amorphous TiO_2 (Am-TiO_2, 9%). Toxic NO_2 is significantly suppressed on HB-TiO_2 with a selectivity of 97%. Moreover, the modulation of defect states allows HB-TiO_2 with a remarkably stable NO removal performance compared to amorphous TiO_2. This study demonstrates that engineering the defect distribution via boron doping can enable the efficient molecular oxygen activation to $\bullet OH$, thus boosting highly NO oxidation removal.

2. Experimental section

2.1. Chemicals and material

All analytical-grade chemicals and materials were purchased from a commercial company and used without further purification.

2.2. Preparation of Photocatalysts

Yellow amorphous TiO_2 (Am-TiO_2) was prepared by the sol-gel procedure [25,26]. 8 g $TiOSO_4$ was added into the 200 mL of deionized water to obtain a transparent Ti^{3+} solution. $NH_3 \bullet H_2O$ was added into above Ti^{3+} solution until the pH value reached to 10, resulting in a white precipitate. Then, the washed precipitate was added to 80 mL of deionized water and 20 mL of 30 wt% H_2O_2 solution. The mixture was stirred for 90 minutes before transferring to a 100 mL Teflon-lined autoclave and heated at 333 K for 12 h. After naturally cooling down to 298 K, the collected yellow gel was dried to yellow powder at 353 K for 8 h. Finally, yellow powder was washed with the deionized water several times and dried overnight. The dried yellow powder was marked as Am-TiO_2. Homogeneous boron-doped amorphous titanium dioxide (HB-TiO_2) was prepared as follows: H_3BO_3 (0.1 M) was added into 50 mL of hot water (~373 K) to form a clear solution with magnetic stirring. Then, 0.5 g Am-TiO_2 was taken into H_3BO_3 solution. After magnetic stirring for 30 min, the mixture was conducted by hydrothermal reaction at 373 K for 10 h. The collected precipitate was washed with hot water after cooling down naturally, and then dried overnight. The obtained powder was marked as HB-TiO_2. HB-TiO_2 with different B contents was obtained by adjusting the concentration of the H_3BO_3 solution (1, 1.5 and 2.5 mol L^{-1}), which were denoted as HB-TiO_2-1, HB-TiO_2-1.5, and HB-TiO_2-2.5, respectively.

3. Results and discussion

3.1. Theoretical calculation analysis

Density functional theory (DFT) calculations were performed to investigate the rearrangement of oxygen defect distribution induced by B doping. The amorphous structure was constructed by pulling out oxygen atoms from the surface and bulk of TiO_2, respectively (Fig. 1a, b). After structure optimization, unsaturated Ti^{3+}, a form of oxygen vacancy, was reconstructed on both surface and bulk phase of amorphous TiO_2 (Fig. 1b). The resulting unsaturated Ti^{3+} exhibits as a five-coordinated asymmetric configuration. As for surface Ti^{3+} sites, H_3BO_3 interacts with them due to the Lewis acid-base interaction, forming a bridged six-coordinated conjugated structure (Figure S1). In this structure, the loss of electrons on B atom and the accumulation of electrons on O atom indicate the electron transfer from B to Ti^{3+} through the Ti-O-B bond (Fig. 1c). Ti^{3+} with electron accumulation can further promote the electron-rich molecular oxygen activation. As the free-state B atom penetrates into the bulk phase of TiO_2, the bulk oxygen vacancy would be filled with these B atoms, meanwhile, the adjacent Ti^{3+} is converted to Ti^{4+} through transferring electrons to B. Because of the electronegativity difference, B preferentially passes the accepted electrons to the neighboring B-O bond. B doping in bulk defect destabilizes the local charge accumulation of the bulk phase, making it feasible for suppressing the recombination of electron and hole. Based on the density of states, pristine TiO_2 shows a bandgap of 2.17 eV, where the valence band (VB) and conduction band (CB) are composed of O 2p orbitals and Ti 3d orbitals, respectively (Fig. 1d). Amorphization of TiO_2 leads to the formation of oxygen vacancies (OV). Thus, oxygen vacancies induce the donor states between the VB and CB, which decreases the bandgap (1.62 eV) of Am-TiO_2 (Fig. 1e), implying a wider range of light absorption. After B doping, the defects of Am-TiO_2 allow to be redistributed, the bandgap is further increased to 1.63 eV (Fig. 1f). More importantly, the spin-symmetric defect levels are incorporated into the VB, indicating that defect of Am-TiO_2 is substituted by B modification. The above difference charge analysis and DOS calculations theoretically verified that B doping can regulate the defect distribution and intrinsic electron transfer of amorphous TiO_2.

3.2. Chemical structure characterization

To check the defect redistribution of amorphous TiO_2 by B doping, homogeneous B-doped TiO_2 (HB-TiO_2) was synthesized using the hydrothermal method (Fig. 2a). As revealed by TEM investigations, Am-TiO_2 and HB-TiO_2 were in the form of sheet and particle, respectively (Figure S2). Am-TiO_2 presented the disordered crystallites (Fig. 2b, White dashed line area). The corresponding SAED pattern displayed a typical diffraction halo, confirming the amorphous structure of Am-TiO_2. Differently, the SAED pattern of HB-TiO_2 exhibited the polycrystalline rings, corresponding to (101), (112), and (200) faces of anatase, indicating that HB-TiO_2 contained a large number of nanocrystals (Fig. 2c). And the shallow halo under the (101) ring reflected the amorphous feature of HB-TiO_2, which may result from the lattice defects of amorphous TiO_2. The (101) plane spacing of 0.354 nm was consistent with anatase, accompanying by some disordered-arranged lattice fringes (Fig. 2d, White dashed line area) [27]. The EDX elemental mapping of HB-TiO_2 clearly showed a uniform distribution of B elements on the surface, demonstrating the modification of H_3BO_3 (Fig. 2e). The nitrogen adsorption-desorption experiments of Am-TiO_2 and HB-TiO_2 exhibited IV curves with H4-type hysteresis loops (Figure S3). Compared with Am-TiO_2 (16.0 m^2 g^{-1}), the specific surface area (137.9 m^2 g^{-1}) of HB-TiO_2 was much larger due to the porous fissure structure, thereby facilitating the adsorption of O_2 and NO. According to XRD patterns, the
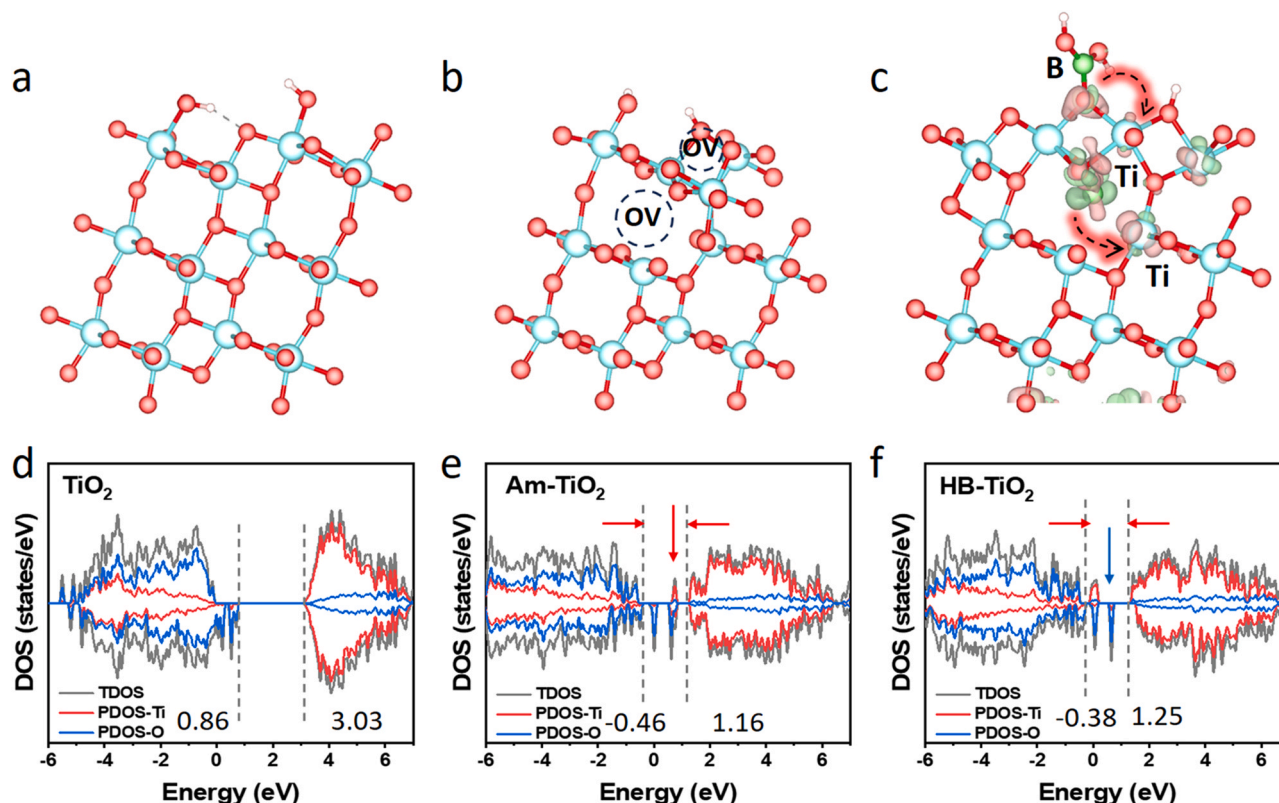
Fig. 1. Optimized theoretical structure of (a) TiO_2 and (b) amorphous TiO_2. (c) The corresponding difference charge analysis of HB-TiO_2. The pink and green regions represent charge accumulation and depletion, respectively. Density of states for (d) TiO_2, (e) Am-TiO_2, (f) HB-TiO_2.

crystalline peaks of Am-TiO_2 were feeble because of the amorphous structure. HB-TiO_2 displayed the indexed planes of (101), (103), (200) and (105), respectively, corresponding to JCPDS 01–0562 (Fig. 2f). Correspondingly, Raman peak of Am-TiO_2 disappeared due to the amorphous structure, while HB-TiO_2 showed the characteristic peaks of anatase at 149, 401, 516 and 639 cm^{-1}, assigning to the E_g, A_{1g} and B_{1g} modes (Fig. 2g). Combining the TEM, XRD and Raman results, Am-TiO_2 owned a complete amorphous structure and HB-TiO_2 underwent the crystallization transformation by B doping that can be identified as a mixture of the amorphous state and the crystalline state. Furthermore, IR peaks at 1600 and 1320 cm^{-1} appeared on HB-TiO_2, corresponding to Ti-OH and B-O-H stretching, respectively (Fig. 2h) [28]. This new B-O-H band further demonstrated the interaction between H_3BO_3 and amorphous TiO_2.

In order to further explore the effect of H_3BO_3 on the defective structure of amorphous TiO_2, the low-temperature electron paramagnetic resonance (EPR) was used to analyze the defect state of Am-TiO_2 and HB-TiO_2. As shown in Fig. 3a, Am-TiO_2 displayed stronger EPR intensity of Ti^{3+} with three characteristic signals at $g_1=2.002$, $g_2=2.007$ and $g_3=2.008$. The $g_4=2.022$ was corresponded to the adsorption of oxygen species (O_2^-/O^-), which were derived from H_2O_2 pretreatment in the precursor synthesis [29,30]. After boronizing to Am-TiO_2, the signal intensity of Ti^{3+} was weakened, indicating that some defect sites can be filled by boric acid or tiny boron atoms. The XPS survey spectra of HB-TiO_2 showed a peak of B, which was indicative of B dopant on TiO_2 (Figure S4). In the high-resolution Ti 2p spectra of Am-TiO_2, the peaks at 459.0 and 464.7 eV can be attributed to $2p_{3/2}$ and $2p_{1/2}$ of Ti^{4+} states, respectively (Figure S5a). Additionally, the peaks at 458.5 and 463.7 eV were observed on Am-TiO_2, assigning to Ti^{3+} states [31]. The Ti^{3+}/Ti^{4+} area ratio of Am-TiO_2 was determined to about 31.1%. The result of defect quantification was consistent with the O 2p XPS analysis. The high-resolution O 2p spectra of Am-TiO_2 could be attributed to lattice oxygen (OL) at 530.2 eV, oxygen vacancies (OV) at 531.2 eV, and

surface hydroxyl groups (-OH) at 532.3 eV (Figure S5b) [32]. Similar to Am-TiO_2, the Ti^{3+}/Ti^{4+} area ratio of HB-TiO_2 was 20.9%, much lower than that of Am-TiO_2. This verified that defects of HB-TiO_2 were replenished by B doping. XPS depth profiles were then used to investigate the effect of boronizing on the defect distribution of HB-TiO_2. As shown in Fig. 3b, the relative content of Ti^{3+} decreased gradually after Ar^+ sputtering. Meanwhile, O 2p depth profiles exhibited a decrease in the fraction of OV (Fig. 3c). More importantly, B 1 s depth profiles presented a wide peak in the range of 190.0–194.0 eV (Fig. 3d), and the corresponding intensities of B maintained a steady trend within the detection depth range (0–4 nm), indicating that B doping can be evenly distributed in HB-TiO_2 [33,34]. The wide peak can be divided into two overlapping peaks at 192.0 and 193.0 eV (Fig. 3d). The peak at 193.0 eV was attributed to the surface boron state (sur-B, BO_3^{3-}), which was disappeared at 0.5 nm. This indicated that BO_3^{3-} species presented on the HB-TiO_2 surface. The other peak at 192 eV was assigned to free-state B (sus-B) in the interstitial bulk, suggesting that B atoms were doped into the lattice of HB-TiO_2 [35,36]. Based on the above analysis, we concluded that surface oxygen vacancies can be modified by BO_3^{3-} and bulk defects would be occupied by free-state B (Fig. 3e, f). Boric acid modification allowed the redistribution of defects in HB-TiO_2, resulting in the formation of a uniform B-doped amorphous TiO_2.

3.3. Charge carrier dynamics

As for photocatalytic NO removal, the carrier dynamics were first studied in detail. As shown in the UV–vis DRS spectra, both Am-TiO_2 and HB-TiO_2 possessed strong visible light absorption capacity (Fig. 4a). Compared with Am-TiO_2, HB-TiO_2 exhibited a blue shift, which could be attributed to the annihilation of bulk defects [37]. Based on the Kubelka-Munk method, the experimental bandgaps of Am-TiO_2 and HB-TiO_2 were determined to 1.90 and 2.30 eV, respectively (Fig. 4b, c and S6) [38]. Consistently, HB-TiO_2 displayed with a down-shift VB and
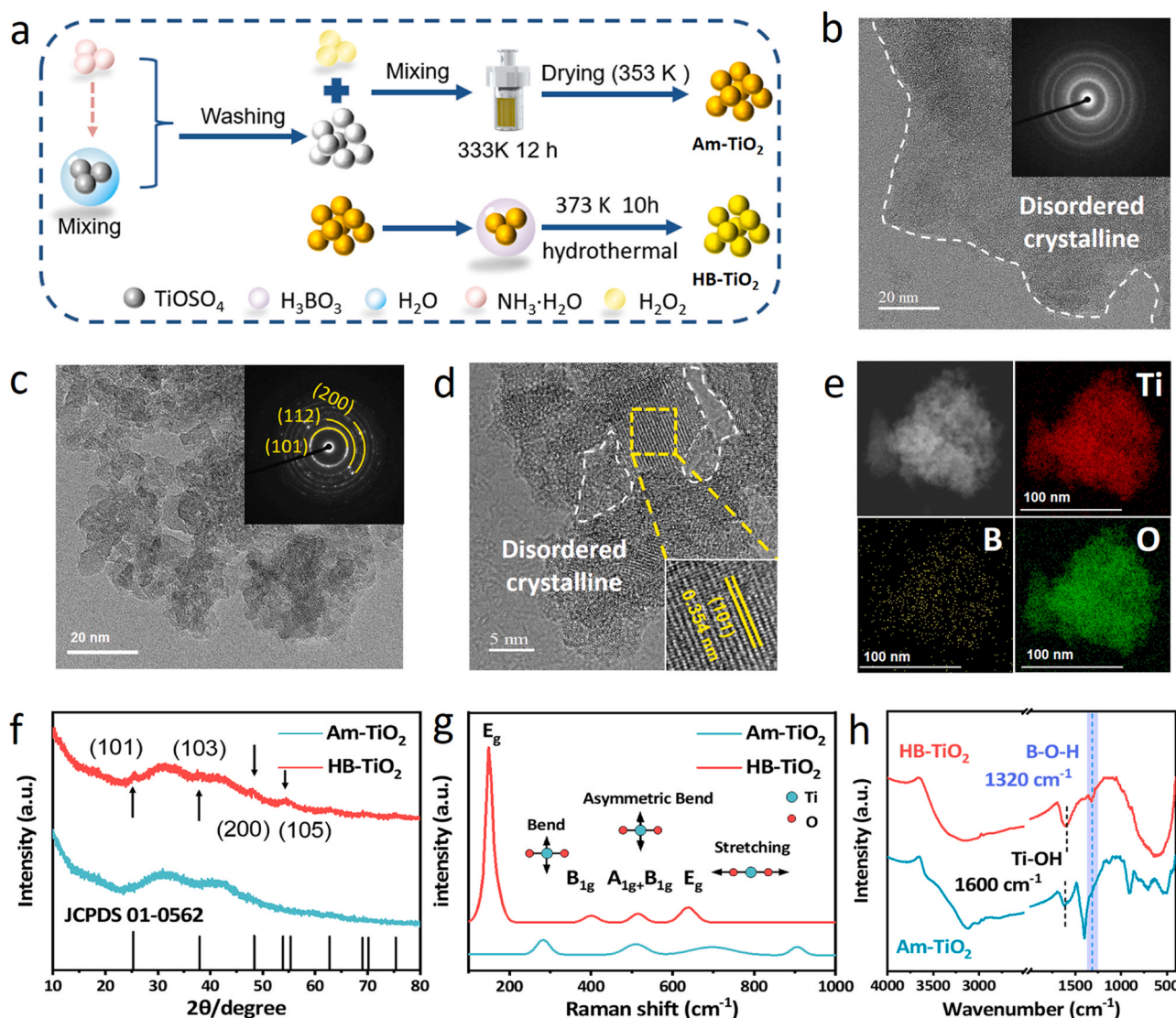
Fig. 2. (a) Synthesis schematic diagram of Am-TiO$_2$ and HB-TiO$_2$. HRTEM images of (b) Am-TiO$_2$ and (c-d) HB-TiO$_2$, the insets in (b) and (c) show the SAED patterns. (e) Corresponding element mapping of HB-TiO$_2$. (f) XRD patterns, (g) Raman spectra and (h) IR spectra of Am-TiO$_2$ and HB-TiO$_2$.

up-shift CB, which amplified its redox capacity. The interfacial charge transfer was further demonstrated by the stable photoluminescence spectra (PL) and time-resolved photoluminescence spectra (Tr-PL). Compared with its counterpart, HB-TiO$_2$ exhibited a weaker PL signal, manifesting the efficient electron-hole separation efficiency (Fig. 4d) [39]. The higher carrier utilization rate of HB-TiO$_2$ can be attributed to B doping that filled up their bulk defects. The corresponding PL decay curves were further applied to get insights into the lifetime of photo-generated carriers (Fig. 4e, f). The average emission lifetime of HB-TiO$_2$ (2.61 ns) was much longer than that of Am-TiO$_2$ (1.66 ns). This implied that abundant electrons and holes can participate in the surface reaction, thus improving photocatalytic activity [39]. In addition, HB-TiO$_2$ showed a higher photocurrent response and the smaller arc radius, favoring the charge separation and transfer (Fig. 4g, h). As aforementioned, boron-doped amorphous TiO$_2$ possesses a strong redox ability and excellent charge transport kinetics, which can facilitate the formation of ROS for efficient NO oxidation removal.

3.4. Photocatalytic NO removal and active species determination

As mentioned above, the enhanced molecular oxygen activation can be achieved by regulating the defect distribution of defective amorphous TiO$_2$ through B doping. Photocatalytic NO removal was then performed on Am-TiO$_2$ and HB-TiO$_2$ using a continuous flow reactor. Upon the visible light irradiation, the NO removal of HB-TiO$_2$ highly increased to 50% within 5 min, while the activity of Am-TiO$_2$ increased to 38% and immediately decreased to 9% (Fig. 5a and S7). For toxic NO$_2$ generation, HB-TiO$_2$ suppressed the by-product NO$_2$ (<10 ppb), resulting in higher reaction selectivity (~97%) compared with Am-TiO$_2$ (Fig. 5b and S7). The performance of photocatalytic NO oxidation removal is closely related to the reaction parameters, such as reaction gas flow rate, reaction gas concentration, reaction chamber size, catalyst contact surface, light intensity, etc. The reaction parameters were changed (as shown in Table S1) and showed that the NO removal efficiency of HB-TiO$_2$ could reach about 92%, which was much higher than that of conventional Am-TiO$_2$ (10%) (Figure S8). Especially, when the concentration of NO was 100 ppb, the removal efficiency of HB-TiO$_2$ was as high as 77%, indicating a good environmental adaptability for the polluted indoors and outdoors. Besides, HB-TiO$_2$ also exhibited good stability. After five cycles, the activity of Am-TiO$_2$ was reduced to 4%. By contrast, photocatalytic NO removal performance of HB-TiO$_2$ presented a slight decrease in activity due to the modification of H$_3$BO$_3$ (Fig. 5c and S9) [40]. To reveal the important role of ROS in NO oxidation, trapping experiments for the primary reactive species were conducted in
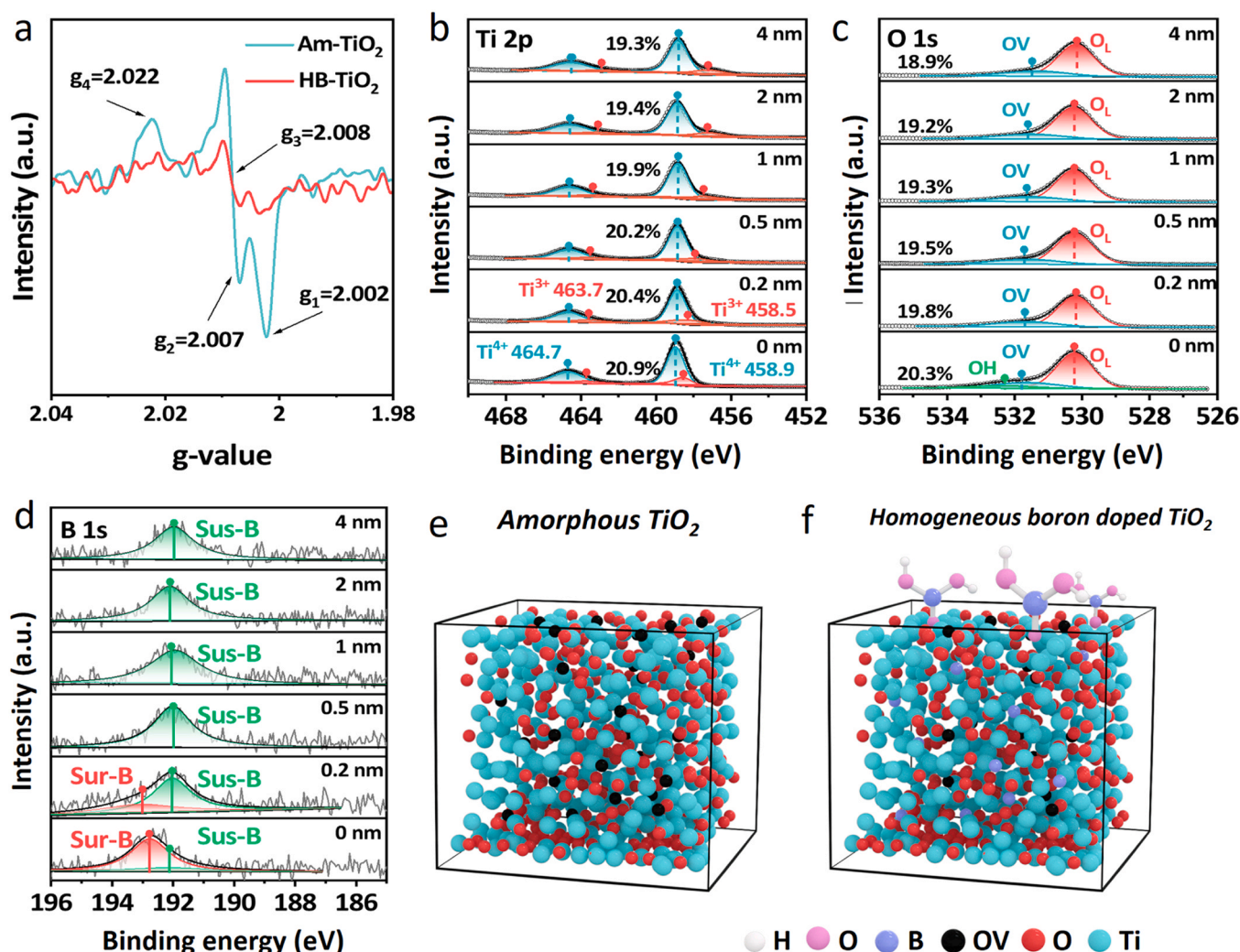
Fig. 3. (a) EPR spectra of Am-TiO$_2$ and HB-TiO$_2$. (b) High-resolution Ti 2p XPS depth profiles, (c) high-resolution O1s XPS depth profiles and (d) high-resolution B 1 s XPS depth profiles of HB-TiO$_2$. Structural schematic illustrations of (e) Am-TiO$_2$ and (f) HB-TiO$_2$.

photocatalytic NO removal (Fig. 5d and S10) [12]. The activity of Am-TiO$_2$ was inhibited by all scavengers. Among them, H$_2$O$_2$ scavenger (catalase) and ^{1}O$_2$ scavenger (L-histidine) completely inhibited the photocatalytic NO removal of Am-TiO$_2$, demonstrating that H$_2$O$_2$ and ^{1}O$_2$ were the critical ROS for NO oxidation (Fig. 5d). Different from Am-TiO$_2$, h$^+$ and •OH were the main active substances with the high inhibition effect. •O$_2^-$, H$_2$O$_2$ and ^{1}O$_2$ scavengers showed a negligible inhibition effect on NO removal, further confirming the superiority of •OH. Notably, the trapping of ^{1}O$_2$ can suppress the formation of NO$_2$, indicating that ^{1}O$_2$ was responsible for NO$_2$ generation. According to the band structure of HB-TiO$_2$, valence band potential cannot meet for the formation of •OH through H$_2$O oxidation. Therefore, we believe that •OH can be formed through molecular oxygen activation, where H$_2$O$_2$ can be decomposed into abundant •OH [41].

Additionally, EPR measurements were conducted to check the production of ROS (•OH, ^{1}O$_2$). In the HB-TiO$_2$ sample, •OH was the main active species for NO oxidation and its signal was much stronger than that of Am-TiO$_2$ (Fig. 5e). On the contrary, the yields of ^{1}O$_2$ and H$_2$O$_2$ on HB-TiO$_2$ were lower than those of Am-TiO$_2$ (Fig. 5f-g and S11, S12). This result indicated that the pathway for ROS generation was modified by H$_3$BO$_3$ treatment. HB-TiO$_2$ was beneficial to activate molecular oxygen to produce H$_2$O$_2$ and quickly decompose H$_2$O$_2$ into •OH. The temperature-programmed desorption (TPD) experiments of O$_2$ and NO were used to investigate the adsorption of reactant molecules. As for O$_2$

adsorption, both Am-TiO$_2$ and HB-TiO$_2$ displayed three peaks in 350–700 K, which can be assigned to physical adsorption (~390 K) and chemisorption (500–650 K) (Fig. 5h). Obviously, HB-TiO$_2$ possessed a superior adsorption ability of O$_2$ because of its higher chemisorption temperature. Compared with O$_2$ adsorption, NO adsorption was weaker on Am-TiO$_2$ and HB-TiO$_2$ (Fig. 5i). This suggested that O$_2$ would be preferentially adsorbed on Am-TiO$_2$ and HB-TiO$_2$, rather than NO. NO oxidation induced by Am-TiO$_2$ and HB-TiO$_2$ catalysts was inclined to undergo Eley-Rideal (E-R) mechanism where adsorbed O$_2$ reacted with free NO to produce nitrate [42].

3.5. Photocatalytic NO oxidation mechanism

In situ DRIFTS spectroscopy was used to dynamically monitor the intermediates and products during the photocatalytic NO oxidation reaction over Am-TiO$_2$ and HB-TiO$_2$. Under the dark conditions, the peaks of monodentate nitrite (1070 cm^{-1}), bidentate nitrite (1118 cm^{-1}) and bridging nitrite (1470 cm^{-1}) appeared on the surface of Am-TiO$_2$ after introducing NO and air into the reaction chamber (Fig. 6a) [16,43]. These nitrites were mainly derived from the reaction of NO with -OH or adsorbed O$_2$. Upon visible light irradiation, the peaks of NO$_2$ (1352 cm^{-1}) and nitrate (1535 cm^{-1}) increased rapidly (Fig. 6b), suggesting that NO$_2$ and nitrate were the main products of NO oxidation reaction on Am-TiO$_2$ [44,45]. In addition, the peaks centered at 1070,
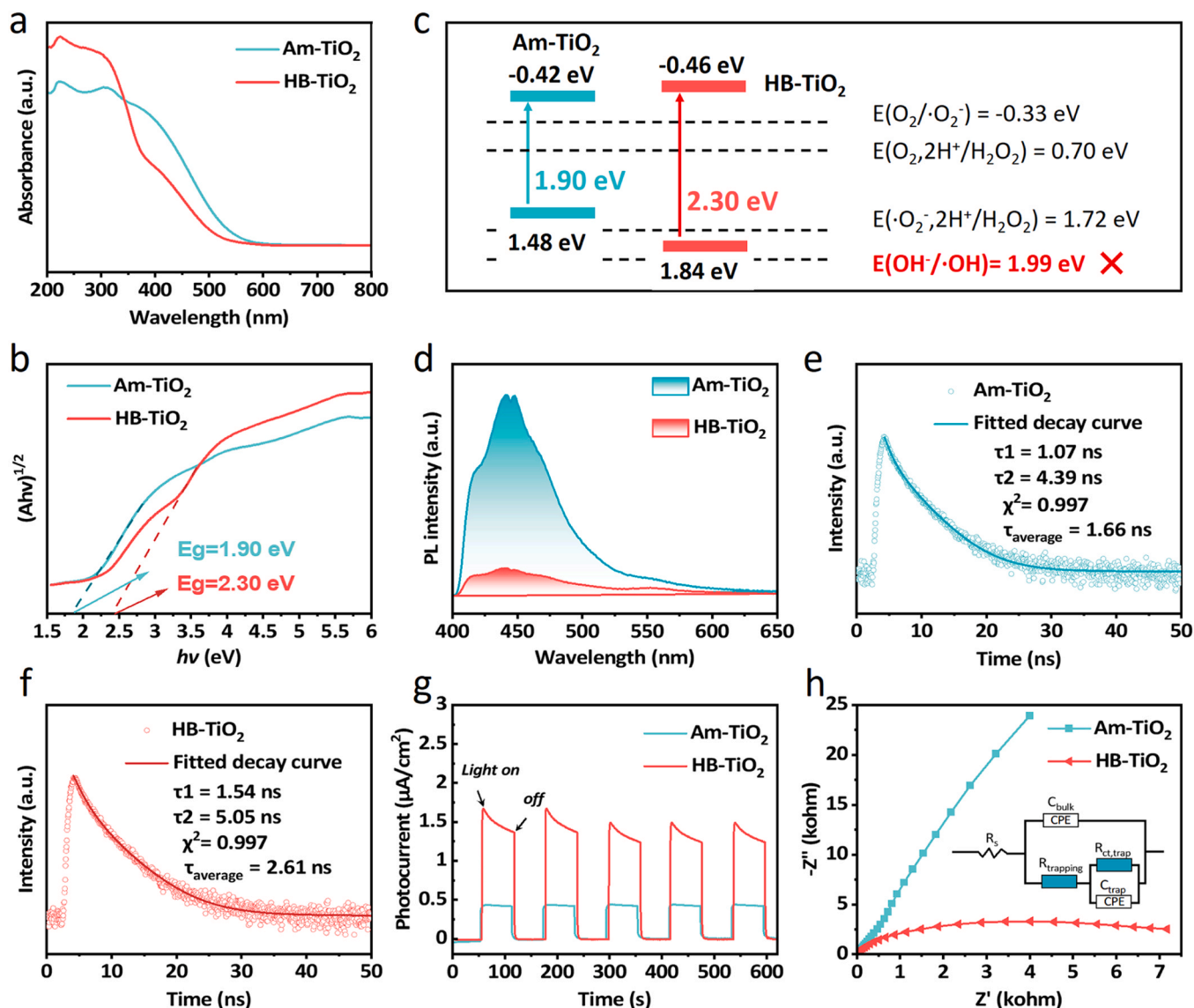
Fig. 4. (a) UV–vis DRS spectra, (b) Corresponding plots of transformed Kubelka-Munk function versus photon energy and (c) the schematic diagram of band structures of Am-TiO$_2$ and HB-TiO$_2$. (d) Room-temperature steady-state PL spectra. The corresponding PL decay curves of (e) Am-TiO$_2$ and (f) HB-TiO$_2$. (g) Transient photocurrent responses and (h) EIS of as-prepared Am-TiO$_2$ and HB-TiO$_2$.

1138 and 1212 cm^{-1} were assigned to monodentate nitrite, bidentate nitrate and NO$^-$, respectively [43]. The peak at 3638 cm^{-1} represented the surface -OH, and its continuous consumption indicated that the surface -OH participated in the NO oxidation (NO + •OH → NO$_2^-$ + H$^+$, 2NO + 2•OH + ^{1}O$_2$ → 2NO$_3^-$ + 2 H$^+$). Notably, there was an increasing characteristic peak (940 cm^{-1}) on Am-TiO$_2$, assigning to the surface adsorbs peroxy-ions [46], indicating the formation of H$_2$O$_2$ during the photo-reaction process. Besides, the formation of nitrate (1535 cm^{-1}) was linearly correlated with the accumulation of H$_2$O$_2$ (940 cm^{-1}) (Figure S13a). This result indicated that H$_2$O$_2$ can be the primary active species for photocatalytic NO removal on Am-TiO$_2$ (NO + O$_2^{2-}$ → NO$_3^-$ + e), which was consistent with the trapping experiments. In the dark reaction of HB-TiO$_2$, the peaks of NO$_2$ and nitrite were detected on the surface of HB-TiO$_2$, those peaks were centered at 1070, 1129, 1300–1600 cm^{-1} (Fig. 6c) [47]. Meanwhile, an increasing peak of free -OH was observed at 3692 cm^{-1}, which could be due to the adsorption of H$_2$O in the air on the surface of the catalyst. Upon visible light irradiation, the peaks of intermediates at 1075 (mon-NO$_2^-$), 1128 (bid-NO$_2^-$), 1352 (NO$_2$), 1441 (mon-NO$_3^-$), 1535 cm^{-1} (bid-NO$_3^-$) were observed on the surface of HB-TiO$_2$ (Fig. 6d) [48]. Notably, a significant decrease in

the IR intensity of NO$_2$ (1352 cm^{-1}) indicated that by-products were suppressed on HB-TiO$_2$ [49]. The peak at 1713 cm^{-1} can be assigned to NO$^+$ that was produced by hole oxidation of adsorbed NO on the surface of HB-TiO$_2$ [14,50]. Although the peak of H$_2$O$_2$ was not detected, the peak of the newly formed -OH group at 3688 cm^{-1} was monitored on HB-TiO$_2$ [51]. Similarly, there was a good linear between •OH radicals (3688 cm^{-1}) and nitrate products (1535 cm^{-1}), indicating that •OH was responsible for the deep oxidation of NO into nitrate on HB-TiO$_2$ (NO$^+$ + 2•OH → NO$_3^-$ + 2 H$^+$) (Figure S13b).

Based on above analysis, Am-TiO$_2$ induced the O$_2$ reduction to generate H$_2$O$_2$ and ^{1}O$_2$, where these species were responsible for NO oxidation to nitrate and NO$_2$ (Fig. 6e). Due to its weak oxidation capacity, ^{1}O$_2$ could cause the partial oxidation of NO to NO$_2$. Boratization can modify the electronic structure of oxygen vacancy on HB-TiO$_2$, which activated O$_2$ to produce H$_2$O$_2$ and immediately promotes the decomposition of H$_2$O$_2$ to produce a large number of •OH. The abundant •OH achieved the complete oxidation of NO. Since the excitonic effect was weakened by the rapid separation of charge carriers induced by boronizing, ^{1}O$_2$ generation was reduced, which further inhibited the production of by-products NO$_2$ [34].
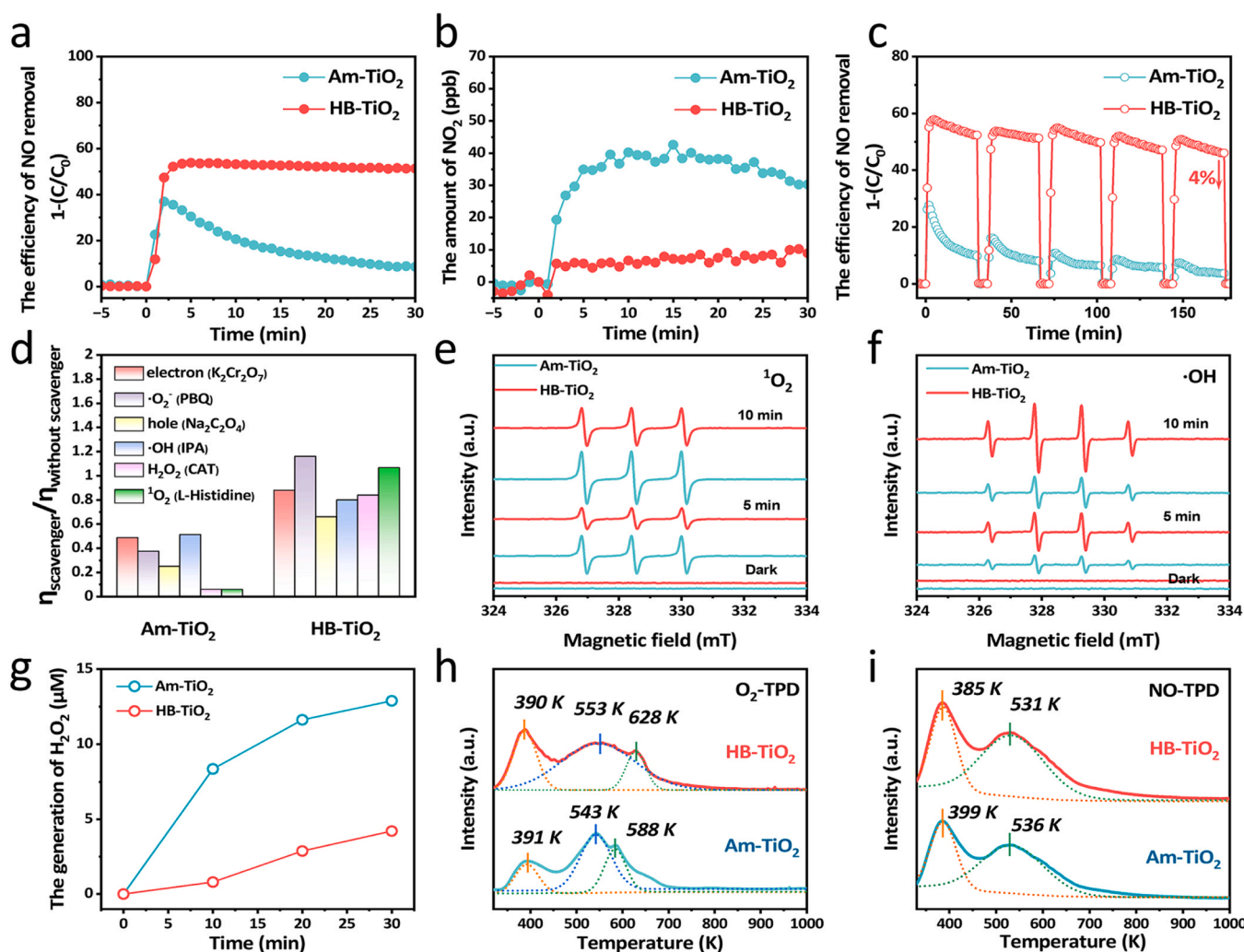
Fig. 5. (a) Photocatalytic NO removal on Am-TiO$_2$ and HB-TiO$_2$ and (b) corresponding generation amount of NO$_2$. (c) Long-term photocatalytic NO removal. (d) Trapping experiments. Detection of active species. EPR spectra of (e) •OH and (f) ^{1}O$_2$. (g) Quantitative detection of H$_2$O$_2$ on Am-TiO$_2$ and HB-TiO$_2$. (h) O$_2$-TPD and (i) NO-TPD of the Am-TiO$_2$ and HB-TiO$_2$.

4. Conclusion

In this study, the homogeneous boron-doped HB-TiO$_2$ photocatalyst was developed to efficiently remove NO pollutant. Theoretical calculation and XPS results indicated that the oxygen defect distribution of the amorphous HB-TiO$_2$ were regulated by B doping, which allowed HB-TiO$_2$ with abundant surface oxygen vacancies. The band structure of HB-TiO$_2$ was modified by oxygen vacancy and B doping, where their intermediate defect levels could promote electron transfer and lengthen electron lifetime. The photocatalytic performance of HB-TiO$_2$ (50%) was increased by five-fold compared with Am-TiO$_2$ (9%). Toxic NO$_2$ was significantly suppressed on HB-TiO$_2$ with a selectivity of 97%. Moreover, HB-TiO$_2$ remained the superior selectivity and activity of NO oxidation after five cycles, indicating that H$_3$BO$_3$ modification could significantly improve the performance instability of amorphous TiO$_2$. Efficient NO removal was ascribed to the cooperation of boron doping and oxygen vacancy. Boron dopants can alter ROS generation to •OH by modulating oxygen defects distribution, thereby boosting the NO oxidation removal. This study can propose new insights into the rational design of catalysts for efficient photocatalytic NO removal through engineering the defect distribution.

CRediT authorship contribution statement

Ding Wang: Methodology, Investigation, Funding acquisition. **Guisheng Li:** Writing – review & editing, Writing – original draft, Supervision, Methodology, Investigation, Funding acquisition, Conceptualization. **Shuangjun Li:** Methodology, Investigation. **Dieqing Zhang:** Writing – review & editing, Writing – original draft, Visualization, Validation, Supervision, Methodology, Investigation, Funding acquisition, Formal analysis, Data curation, Conceptualization. **Qing Wang:** Methodology, Investigation. **Shike Wang:** Methodology, Investigation. **Jinghuan Peng:** Methodology, Investigation. **Xichen Feng:** Methodology, Investigation. **Pengpeng Li:** Methodology, Investigation. **Hui Xu:** Methodology, Investigation. **Chengliang Mao:** Methodology, Investigation. **Hongbao Jia:** Writing – review & editing, Writing – original draft, Visualization, Methodology, Investigation, Formal analysis, Data curation, Conceptualization. **Hao Li:** Methodology, Investigation, Conceptualization. **Huan Shang:** Writing – review & editing, Writing – original draft, Visualization, Validation, Supervision, Methodology, Investigation, Funding acquisition, Formal analysis, Data curation, Conceptualization. **Shuning Xiao:** Methodology, Investigation, Funding acquisition. **Yue He:** Visualization, Methodology, Investigation. **Shuwei Gu:** Visualization, Validation, Methodology, Investigation.
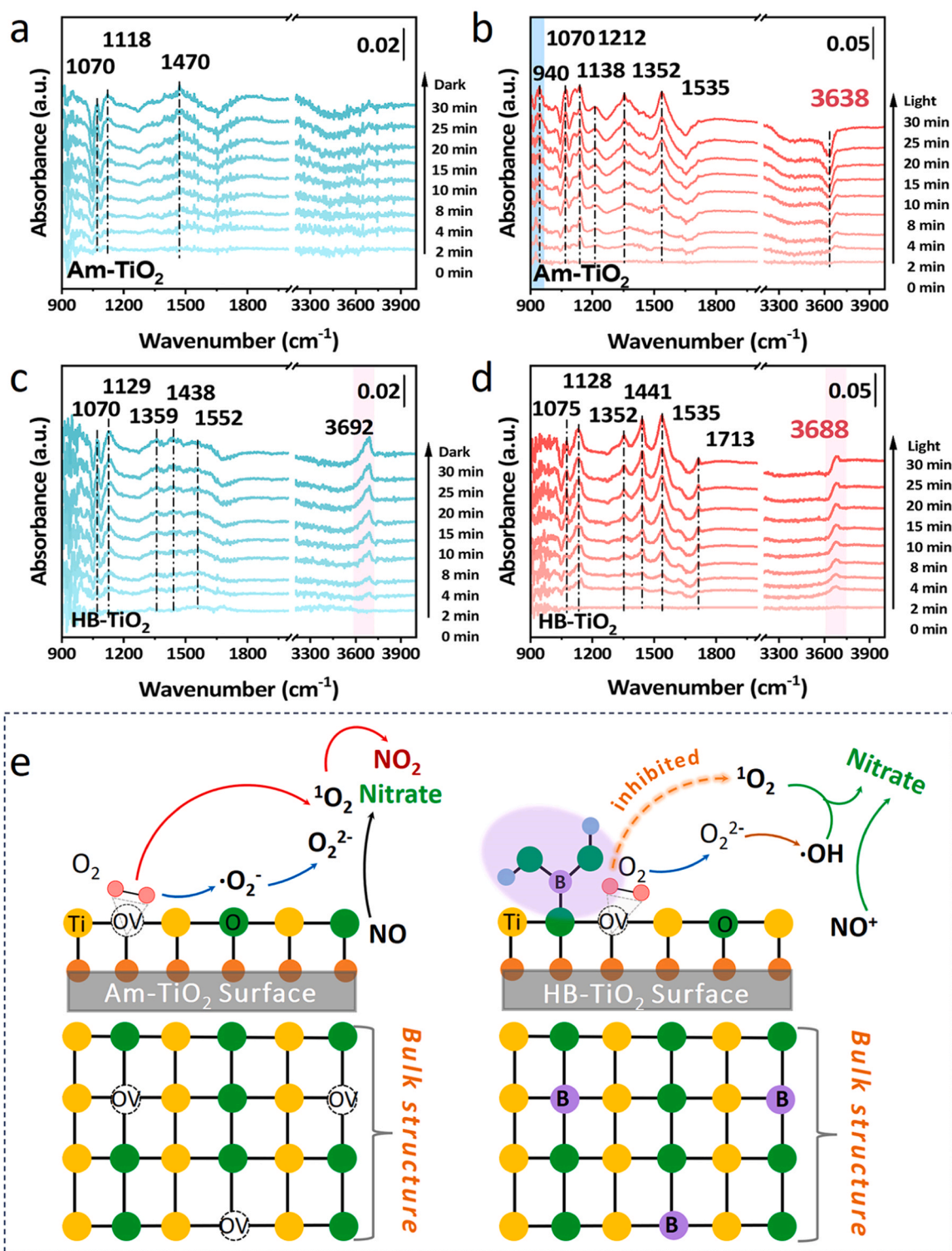
Fig. 6. *In situ* FTIR spectra of (a) Am-TiO$_2$ and (c) HB-TiO$_2$ for NO and O$_2$ adsorption. *In situ* FTIR of (b) Am-TiO$_2$ and (d) HB-TiO$_2$ for the NO oxidation reaction. (e) Schematic illustration of the interfacial molecular oxygen activation and NO oxidation mechanism on Am-TiO$_2$ and HB- TiO$_2$, respectively.

Declaration of Competing Interest

The authors declare that they have no known competing financial interests or personal relationships that could have appeared to influence the work reported in this paper.

Data Availability

Data will be made available on request.

Acknowledgments

Author Contributions

H.J. and H.S. contributed equally. The article was written through contributions of all authors. All authors have given approval to the final version of the manuscript.

Appendix A. Supporting information

Supplementary data associated with this article can be found in the online version at doi:10.1016/j.apcatb.2024.124239.

References

[1] V. Khanal, N.O. Balayeva, C. Günnemann, Z. Mamiyev, R. Dillert, D. W. Bahnemann, V. Subramanian, Photocatalytic NO_x removal using tantalum oxide nanoparticles: a benign pathway, Appl. Catal. B Environ. 291 (2021) 119974.

[2] A. Pastor, F. Rodriguez-Rivas, Gd Miguel, M. Cruz-Yusta, F. Martin, I. Pavlovic, L. Sánchez, Effects of Fe^{3+} substitution on Zn-Al layered double hydroxides for enhanced NO photochemical abatement, Chem. Eng. J. 387 (2020) 124110.

[3] J.L. Laughner, R.C. Cohen, Direct observation of changing NO_x lifetime in North American cities, Science 366 (2019) 723–727.

[4] S.C. Anenberg, J. Miller, R. Minjares, L. Du, D.K. Henze, F. Lacey, C.S. Malley, L. Emberson, V. Franco, Z. Klimont, C. Heyes, Impacts and mitigation of excess diesel-related NO_x emissions in 11 major vehicle markets, Nature 545 (2017) 467–471.

[5] H.M.A. Sharif, M. Ali, A. Mahmood, M.B. Asif, M.A.U. Din, M. Sillanpää, A. Mahmood, B. Yang, Separation of Fe from wastewater and its use for NO_x reduction; a sustainable approach for environmental remediation, Chemosphere 303 (2022) 135103.

[6] H.M.A. Sharif, M.B. Asif, Y. Wang, Y.-N. Hou, B. Yang, X. Xiao, C. Li, Spontaneous intra-electron transfer within $rGO@Fe_2O_3$-MnO catalyst promotes long-term NO_x reduction at ambient conditions, J. Hazard. Mater. 441 (2023) 129951.

[7] H.M.A. Sharif, M.B. Asif, Y. Wang, K. Khan, Y. Cai, X. Xiao, C. Li, Construction and elucidation of zerovalent iron@terephthalic acid/iron oxide catalyst to activate peroxymonosulfate for accelerating and long-lasting NO_x removal, Chem. Eng. J. 465 (2023) 142782.

[8] H. Xu, X. Liu, H. Li, L. Zhang, O_2 activation and $^1O_2$ generation over phosphate modified BiOCl for efficient photodegradation of organic pollutants, Appl. Catal. B Environ. 314 (2022) 121520.

[9] S. Zhao, Y. Yang, F. Bi, Y. Chen, M. Wu, X. Zhang, G. Wang, Oxygen vacancies in the catalyst: efficient degradation of gaseous pollutants, Chem. Eng. J. 454 (2023) 140376.

[10] F.R. Guo, C.L. Mao, C. Liang, P. Xing, L.H. Yu, Y.B. Shi, S.Y. Cao, F.Y. Wang, X. Liu, Z.H. Ai, L.Z. Zhang, Triangle $Cl-Ag_1-Cl$ sites for superior photocatalytic molecular oxygen activation and NO oxidation of BiOCl, Angew. Chem. Int. Ed. 62 (2023) e202314243.

[11] W. Dai, S. Zhang, H. Shang, S. Xiao, Z. Tian, W. Fan, X. Chen, S. Wang, W. Chen, D. Zhang, Breaking the selectivity barrier: reactive oxygen species control in photocatalytic nitric oxide conversion, Adv. Funct. Mater. 34 (2023) 2309426.

[12] H. Shang, H. Jia, P. Li, H. Li, W. Zhang, S. Li, Q. Wang, S. Xiao, D. Wang, G. Li, D. Zhang, Highly selective and efficient photocatalytic NO removal: charge carrier kinetics and interface molecular process, Nano Res 17 (2024) 1003–1026.

[13] S. Wang, W. Cui, B. Lei, X.A. Dong, Y. Tang, F. Dong, Targeted NO oxidation and synchronous NO_2 inhibition via oriented $^1O_2$ formation based on lewis acid site adjustment, Environ. Sci. Technol. 57 (2023) 12890–12900.

[14] X. Song, W. Jiang, Z. Cai, X. Yue, X. Chen, W. Dai, X. Fu, Visible light-driven deep oxidation of NO and its durability over Fe doped $BaSnO_3$: the NO^+ intermediates mechanism and the storage capacity of Ba ions, Chem. Eng. J. 444 (2022) 136709.

[15] H. Li, H. Shang, X. Cao, Z. Yang, Z. Ai, L. Zhang, Oxygen vacancies mediated complete visible light NO oxidation via side-on bridging superoxide radicals, Environ. Sci. Technol. 52 (2018) 8659–8665.

[16] Q. Li, J. Zhao, H. Shang, Z. Ma, H. Cao, Y. Zhou, G. Li, D. Zhang, H. Li, Singlet oxygen and mobile hydroxyl radicals Co-operating on gas–solid catalytic reaction interfaces for deeply oxidizing NO_x, Environ. Sci. Technol. 56 (2022) 5830–5839.

[17] H. Li, H. Shang, Y. Li, X. Cao, Z. Yang, Z. Ai, L. Zhang, Interfacial charging–decharging strategy for efficient and selective aerobic NO oxidation on oxygen vacancy, Environ. Sci. Technol. 53 (2019) 6964–6971.

[18] S. Li, H. Shang, H. Tao, P. Li, H. Pan, Q. Wang, S. Zhang, H. Jia, H. Zhang, J. Cao, B. Zhang, R. Zhang, G. Li, Y. Zhang, D. Zhang, H. Li, Hydroxyl radical-mediated efficient photoelectrocatalytic NO oxidation with simultaneous nitrate storage using a flow photoanode reactor, Angew. Chem. Int. Ed. 62 (2023) e202305538.

[19] H. Shang, H. Jia, W. Zhang, S. Li, Q. Wang, Q. Yang, C. Zhang, Y. Shi, Y. Wang, P. Li, Y. He, S. Xiao, D. Wang, D. Zhang, Surface hydrogen bond-induced oxygen vacancies of TiO_2 for two-electron molecular oxygen activation and efficient no oxidation, Environ. Sci. Technol. 57 (2023) 20400–20409.

[20] M. Shen, T. Ding, W.H. Rackers, C. Tan, K. Mahmood, M.D. Lew, B. Sadtler, Single-molecule colocalization of redox reactions on semiconductor photocatalysts connects surface heterogeneity and charge-carrier separation in bismuth oxybromide, J. Am. Chem. Soc. 143 (2021) 11393–11403.

[21] H. Li, H. Zhu, Y. Shi, H. Shang, L. Zhang, J. Wang, Vacancy-rich and porous NiFe-layered double hydroxide ultrathin nanosheets for efficient photocatalytic NO oxidation and storage, Environ. Sci. Technol. 56 (2022) 1771–1779.

[22] S. Zhang, X. Yi, G. Hu, M. Chen, H. Shen, B. Li, L. Yang, W. Dai, J. Zou, S. Luo, Configuration regulation of active sites by accurate doping inducing self-adapting defect for enhanced photocatalytic applications: a review, Coord. Chem. Rev. 478 (2023) 214970.

[23] B.-X. Zhou, S.-S. Ding, K.-X. Yang, J. Zhang, G.-F. Huang, A. Pan, W. Hu, K. Li, W. Q. Huang, Generalized synthetic strategy for amorphous transition metal oxides-based 2D heterojunctions with superb photocatalytic hydrogen and oxygen evolution, Adv. Funct. Mater. 31 (2021) 2009230.

[24] Y. Kang, Y. Yang, L.-C. Yin, X. Kang, G. Liu, H.-M. Cheng, An amorphous carbon nitride photocatalyst with greatly extended visible-light-responsive range for photocatalytic hydrogen generation, Adv. Mater. 27 (2015) 4572–4577.

[25] X. Bi, G. Du, D. Sun, M. Zhang, Y. Yu, Q. Su, B. Xu, Room-temperature synthesis of yellow TiO_2 nanoparticles with enhanced photocatalytic properties, Appl. Surf. Sci. 511 (2020) 145617.

[26] M. Shen, M. Wang, Q. Wang, J. Tian, L. Zhang, L. Wang, J. Shi, A Ti-OH bond breaking route for creating oxygen vacancy in titania towards efficient CO_2 photoreduction, Chem. Eng. J. 425 (2021) 131513.

[27] Y. Tao, Z. Ma, W. Wang, C. Zhang, L. Fu, Q. Zhu, Y. Li, G. Li, D. Zhang, Nickel phosphide clusters sensitized TiO_2 nanotube arrays as highly efficient photoanode for photoelectrocatalytic urea oxidation, Adv. Funct. Mater. 33 (2023) 2211169.

[28] B. Wu, X. Jiang, S. Yu, P. Bai, X. Guo, J. Lyu, Unveiling the nature of boric acid adsorption by metal-organic frameworks with hexanuclear clusters, Chem. Eng. J. 433 (2022) 133543.

[29] E. Konstantinova, A. Minnekhanov, A. Beltiukov, V. Ivanov, A.J. Sutherland, O. Boytsova, Unveiling point defects in titania mesocrystals: a combined EPR and XPS study, N. J. Chem. 42 (2018) 15184–15189.

[30] F. Zuo, L. Wang, T. Wu, Z. Zhang, D. Borchardt, P. Feng, Self-doped Ti^{3+} enhanced photocatalyst for hydrogen production under visible light, J. Am. Chem. Soc. 132 (2010) 11856–11857.

[31] Z. Hu, X. Li, S. Zhang, Q. Li, J. Fan, X. Qu, K. Lv, $Fe1/TiO_2$ Hollow microspheres: Fe and Ti dual active sites boosting the photocatalytic oxidation of NO, Small 16 (2020) 2004583.

[32] J. Zhang, H. Tao, S. Wu, J. Yang, M. Zhu, Enhanced durability of nitric oxide removal on TiO_2 (P25) under visible light: enabled by the direct Z-scheme mechanism and enhanced structure defects through coupling with C_3N_5, Appl. Catal. B Environ. 296 (2021) 120372.

[33] J. Cao, Z. Zhang, Xa Dong, H. Fu, X. Zhang, X. Lv, Y. Li, G. Jiang, Defective borate-decorated polymer carbon nitride: enhanced photocatalytic NO removal, synergy effect and reaction pathway, Appl. Catal. B Environ. 249 (2019) 266–274.

[34] Y. Shi, Z. Yang, L. Shi, H. Li, X. Liu, X. Zhang, J. Cheng, C. Liang, S. Cao, F. Guo, X. Liu, Z. Ai, L. Zhang, Surface boronizing can weaken the excitonic effects of BiOBr nanosheets for efficient O_2 activation and selective NO oxidation under visible light irradiation, Environ. Sci. Technol. 56 (2022) 14478–14486.

[35] L. Duan, L. Wang, K.N. Heck, C.A. Clark, J. Wei, M. Wang, J. Metz, G. Wu, A.-L. Tsai, S. Guo, J. Arredondo, A.D. Mohite, T.P. Senftle, P. Westerhoff, P. Alvarez, X. Wen, Y. Song, M.S. Wong, Titanium oxide improves boron nitride photocatalytic degradation of perfluorooctanoic acid, Chem. Eng. J. 448 (2022) 137735.

[36] T. Wei, Z. Fan, G. Zhao, Enhanced adsorption and degradation of nonylphenol on electron-deficient centers of photocatalytic surfaces, Chem. Eng. J. 388 (2020) 124168.

[37] X. Li, K. Li, D. Ding, J. Yan, C. Wang, S.A.C. Carabineiro, Y. Liu, K. Lv, Effect of oxygen vacancies on the photocatalytic activity of flower-like BiOBr microspheres towards NO oxidation and CO_2 reduction, Sep. Purif. Technol. 309 (2023) 123054.

[38] X. Liu, H. Ma, M. Zhang, P. Che, Y. Luo, S. Zhang, J. Xu, Catalytic activation of molecular oxygen toward producing hydroxyl radicals controllably for highly selective oxidation of hydroxyl compounds under mild conditions, ACS Catal. 13 (2023) 11104–11116.

[39] Y. Zhang, Z. Hu, H. Zhang, H. Li, S. Yang, Uncovering original Z-scheme heterojunctions of COF/MO_x (M = Ti, Zn, Zr, Sn, Ce, and Nb) with ascendant photocatalytic selectivity for virtually 99.9% NO-to-NO_3^- oxidation, Adv. Funct. Mater. 33 (2023) 2303851.

[40] H. Ma, X. Wang, T. Tan, X. Zhou, F. Dong, Y. Sun, Stabilize the oxygen vacancies in Bi_2SiO_5 for durable photocatalysis via altering local electronic structure with phosphate dopant, Appl. Catal. B Environ. 319 (2022) 121911.

[41] L. Yang, Z. Chen, Q. Cao, H. Liao, J. Gao, L. Zhang, W. Wei, H. Li, J. Lu, Structural regulation of photocatalyst to optimize hydroxyl radical production pathways for highly efficient photocatalytic oxidation, Adv. Mater. 36 (2023) 2306758.

[42] H. Shang, S. Huang, H. Li, M. Li, S. Zhao, J. Wang, Z. Ai, L. Zhang, Dual-site activation enhanced photocatalytic removal of NO with Au/CeO_2, Chem. Eng. J. 386 (2020) 124047.

[43] H. Ma, Y. He, X. Li, J. Sheng, J. Li, F. Dong, Y. Sun, In situ loading of MoO_3 clusters on ultrathin Bi_2MoO_6 nanosheets for synergistically enhanced photocatalytic NO abatement, Appl. Catal. B Environ. 292 (2021) 120159.

[44] H. Ma, Y. He, Xa Dong, J. Sheng, S. Chen, F. Dong, G. Xie, Y. Sun, Doping and facet effects synergistically mediated interfacial reaction mechanism and selectivity in photocatalytic NO abatement, J. Colloid Interface Sci. 604 (2021) 624–634.

[45] W. Huo, W. Xu, T. Cao, X. Liu, Y. Zhang, F. Dong, Carbonate-intercalated defective bismuth tungstate for efficiently photocatalytic NO removal and promotion mechanism study, Appl. Catal. B Environ. 254 (2019) 206–213.

[46] Y. Nosaka, A.Y. Nosaka, Generation and detection of reactive oxygen species in photocatalysis, Chem. Rev. 117 (2017) 11302–11336.

[47] F. Rao, G. Zhu, W. Zhang, J. Gao, F. Zhang, Y. Huang, M. Hojamberdiev, In-situ generation of oxygen vacancies and metallic bismuth from $(BiO)_2CO_3$ via N_2-assisted thermal-treatment for efficient selective photocatalytic NO removal, Appl. Catal. B Environ. 281 (2021) 119481.

[48] G. Li, Z. Lian, Z. Wan, Z. Liu, J. Qian, Y. Deng, S. Zhang, Q. Zhong, $Ni(OH)_2$ clusters decorated $NiTiO_3$ Z-scheme heterojunctions with strong O_2 activation and robust interfacial built-in electric field for efficient NO photo-oxidation, Chem. Eng. J. 451 (2023) 138625.

[49] Q. Ren, Y. He, H. Wang, Y. Sun, F. Dong, Photo-switchable oxygen vacancy as the dynamic active site in the photocatalytic NO oxidation reaction, ACS Catal. 12 (2022) 14015–14025.

[50] M. Xiong, Y. Tao, Z. Zhao, Q. Zhu, X. Jin, S. Zhang, M. Chen, G. Li, Porous $g-C_3N_4/TiO_2$ foam photocatalytic filter for treating NO indoor gas, Environ. Sci. Nano 8 (2021) 1571–1579.

[51] J.C.S. Wu, Y.T. Cheng, In situ FTIR study of photocatalytic NO reaction on photocatalysts under UV irradiation, J. Catal. 237 (2006) 393–404.